Turbulent Kinetic Energy Analysis Of Coherent Structures In The Near Field Of Constant/Variable Density Jet Flows

F. Patiño[1*], L. Voivenel[1], L. Danaila[1], E. Varea[1]

1: Normandie Univ., UNIROUEN, INSA Rouen, CNRS, CORIA, 76000 Rouen, France
*Corresponding author: francisco.patino@univ-rouen.fr

Keywords: PLIF, PIV, Turbulent Kinetic Energy, Kelvin-Helmholtz Structures, Variable Density Jet, Round Jet, Turbulence.

ABSTRACT

Turbulent round jets exhibit strong intermittency in their shear layers, where localized events govern mixing and energy transfer. Conventional global (whole field) averaging provides robust mean trends, but it can obscure the dynamics of individual events because coherent motions vary in position, orientation and intensity across realizations. In this study we analyse turbulence in the frame of coherent structures: repeatable features that organize local transport over finite spatial regions. Coherent structures are detected by template matching on instantaneous PLIF scalar fields using a correlation criterion, and synchronized PIV fields are extracted at the same locations. Each detection is converted into a fixed size window aligned with the structure, enabling ensemble statistics in a local reference frame that can be compared directly with global averages. Two configurations are considered: a constant density round jet (N2/N2) and a variable density round jet (He/N2) issuing into the same nitrogen coflow. Energetics are quantified using an axisymmetric turbulent kinetic energy (TKE) budget in cylindrical coordinates under statistically stationary, low-Mach-number conditions. Reynolds averages are used for the N2/N2 jet, while Favre averages are used for the He/N2 jet to account for density fluctuations. The evaluated terms are mean flow advection, shear production including anisotropy contributions, radial and axial turbulent transport in divergence form, and dissipation estimated with a two-dimensional locally axisymmetric surrogate. Pressure diffusion, unresolved azimuthal transport and remaining measurement/processing imbalance are grouped into a residual. The results show that structure conditioning sharpens dissipation and production into thin sheets and compact hot spots that are smeared in global averages. Advection and turbulent diffusion, which appear as broad patterns in the laboratory frame, become localized neighboring positive/negative lobes inside the structure frame, revealing event-wise redistribution across and along the turbulent/non-turbulent interface. Increasing Reynolds number intensifies all budget terms, while variable density amplifies asymmetry and enhances the relative importance of transport terms in the helium jet. Normalized local budget bars confirm that the negative side is dominated mainly by dissipation, whereas the positive activity is carried by advection and, depending on position and configuration, by turbulent diffusion or the pressure-diffusion/residual contribution. The structure-conditioned framework therefore separates dynamic structures from background turbulence and provides a compact view of how coherent shear layer events redistribute turbulent kinetic energy in constant and variable density jets.

1. Introduction

Turbulent round jets remain a canonical configuration for studying entrainment, mixing and interfacial transport, yet their near field is strongly intermittent because the dominant shear layer events wander in space and vary from one realisation to another. Whole field averages therefore recover robust mean trends while partly smearing the coherent motions that actually organise momentum and scalar exchange near the turbulent/non-turbulent interface (TNTI). Recent work has shown that entrainment in free shear flows must be connected across local and global descriptions, that the evolution of the turbulence interface is closely linked to nearby coherent vortices, and that intense interscale transfer and dissipation processes concentrate at the interface itself van Reeuwijk et al. (2021); Neamtu-Halic et al. (2020); Zhou & Vassilicos (2020). Motivated by this perspective, the present paper presents an experimental analysis of turbulent kinetic energy (TKE) transport in the near field of round jets using simultaneous PIV/PLIF measurements and structure conditioned averaging. A constant density N_2/N_2 jet and a variable density He/N_2 jet are examined in the same coflow so that intermittency, density contrast and local transport can be compared within a common framework. Coherent structures associated with Kelvin–Helmholtz roll-ups are detected on the instantaneous scalar fields, synchronised velocity patches are extracted around each event, and global statistics are contrasted with averages formed in the local frame of the detected structures.

2. Experimental Setup

The flow facility is composed of a round jet of diameter $D_j = 30\ \mathrm{mm}$ surrounded by a cylindrical coflow of diameter $D_c = 256\ \mathrm{mm}$. The nozzle contraction is designed to provide a top-hat exit profile and a low initial turbulence level, while the large coflow diameter limits confinement effects and permits the jet to develop under well-defined boundary conditions. The coflow velocity is adjusted so that the Craya–Curtet number remains approximately constant, $C_{tni} \simeq 0.7$, across operating points. Two gas configurations are investigated: a constant density nitrogen jet issuing into nitrogen (N_2/N_2), and a variable density helium jet issuing into nitrogen (He/N_2). Nitrogen provides the constant density reference case, whereas helium introduces a strong density contrast while remaining compatible with simultaneous optical measurements.

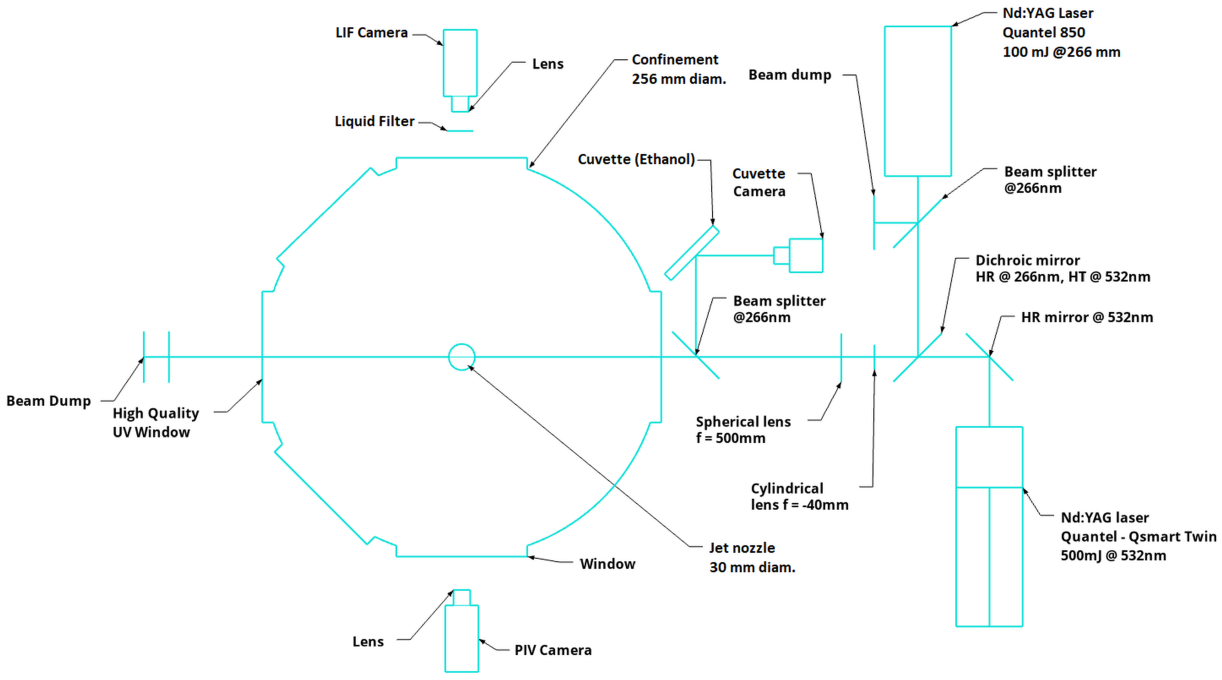


Figure 1. Sketch of the experimental montage for the simultaneous PLIF and PIV measurements. The PIV beam at $532\ \mathrm{nm}$ and the PLIF beam at $266\ \mathrm{nm}$ are combined optically before the laser sheet crosses the jet center plane.

The density and dynamic viscosity ratios are defined as $R_\rho = \rho_j/\rho_c$ and $R_\mu = \mu_j/\mu_c$, where the subscripts j and c refer to the injected jet and the ambient coflow. At $T = 293\ \mathrm{K}$, the present $\mathrm{N_2/N_2}$ configuration has $R_\rho = 1$ and $R_\mu = 1$, while the $\mathrm{He/N_2}$ configuration has $R_\rho \simeq 1/7$ and $R_\mu \simeq 1.13$.

Gas	$\rho\ (\mathrm{kg\,m^{-3}})$	$\mu\ (\mathrm{Pa\,s})$	R_ρ	R_μ
$\mathrm{N_2}$	1.16	1.76×10^{-5}	1	1
He	0.164	1.96×10^{-5}	1/7	1.13

Table 1. Gas properties at $T = 293\ \mathrm{K}$ used to define the constant- and variable-density operating conditions.

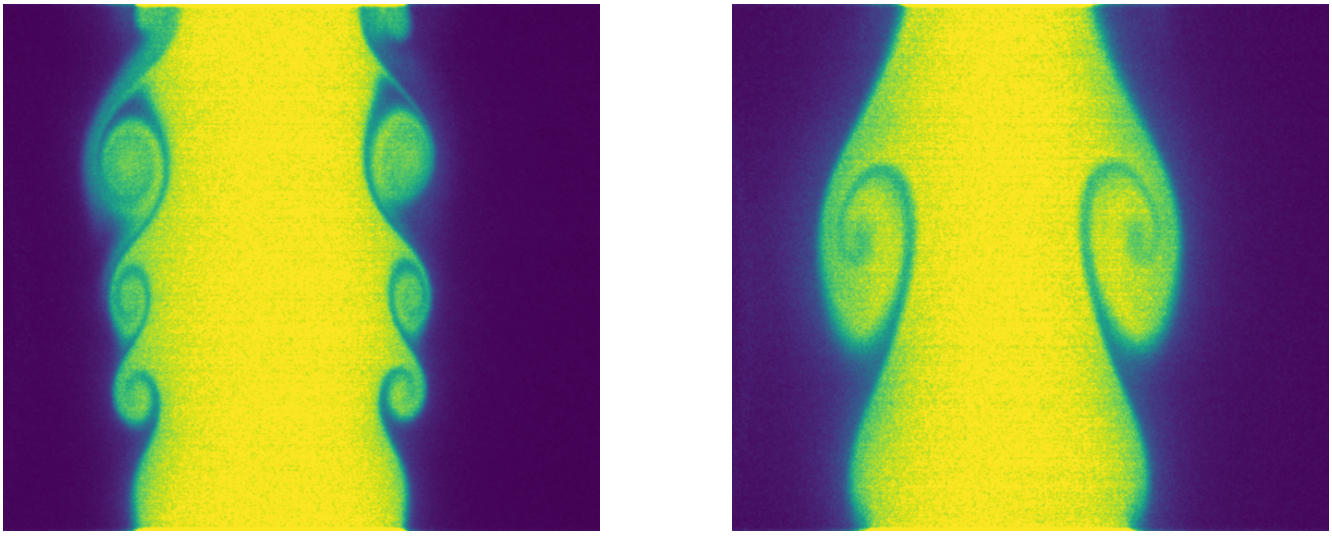
Gas flow rates are imposed with mass-flow controllers. The operating points are obtained by solving the coupled constraints on Reynolds number, Craya–Curtet number and total momentum flux. For $\mathrm{N_2/N_2}$, the Reynolds number is varied directly; for $\mathrm{He/N_2}$, the jet and coflow velocities are chosen so that the momentum flux at the jet exit matches the corresponding nitrogen case. Tables 2 and 3 as well as summarize the operating points used in the present paper and Figure 2 shows the difference of between both jets at the same momentum flux.

N_2			
Re	2000	4000	6000
Fr	0.0000	0.0000	0.0000
u_j (m/s)	1.1228	2.2457	3.3688
u_c (m/s)	0.0635	0.1272	0.1910
Q_{mj} (g/s)	0.9031	1.8062	2.7095
Q_{mc} (g/s)	3.6683	7.3448	11.0294
M_0 (Pa)	1.4354	5.7422	12.9215

Table 2. Flow conditions for the N_2 jet. M_0: momentum flux at the jet exit.

He			
u_j (m/s)	2.9711	5.9426	8.9145
u_c (m/s)	0.0627	0.1255	0.1884
Q_{mj} (g/s)	0.3432	0.6865	1.0299
Q_{mc} (g/s)	3.6232	7.2505	10.8821
Re	720	1440	2160
Fr	0.2087	0.0522	0.0232

Table 3. Flow conditions for the He jet. M_0 values match those in Table 2.



(a) N_2/N_2, Re=4000 **(b)** He/N_2, Re=1440

Figure 2. Comparison between N_2 and He jets at different Reynolds numbers but at a matched momentum of $M_0 = 5.74$.

2.1. PIV measurements

Planar PIV (2D–2C) is employed to measure the in-plane velocity components in the meridional (r, y) plane. A Quantel Ultra Twin pulsed laser at $\lambda = 532\ \mathrm{nm}$ and approximately $150\ \mathrm{mJ}$ per pulse delivers a beam transformed into a parallel laser sheet by a cylindrical lens ($f = -40\ \mathrm{mm}$) followed by a spherical lens ($f = 500\ \mathrm{mm}$). The flow is seeded with Di-Ethyl-Hexyl-Sebacat (DEHS) particles of approximately $1\ \mu\mathrm{m}$ diameter. Mie scattering is recorded by an Imager ProX camera equipped with a Nikkor $105\ \mathrm{mm}$, $f/2.8$ lens. The field of view is $71.86 \times 71.86\ \mathrm{mm}^2$, corresponding to a spatial calibration of approximately $0.0351\ \mathrm{mm/pixel}$. The image pairs are processed with a decreasing multi-pass interrogation strategy down to 12×12 pixel windows with 50% overlap, giving a vector spacing of about $0.211\ \mathrm{mm}$.

The PIV system operates in double-frame mode. The delay between shots is adjusted for each operating point so that the mean particle displacement remains suitable for correlation processing. The resulting delays range from $140\ \mu\mathrm{s}$ to $40\ \mu\mathrm{s}$ in the N_2/N_2 cases and from $55\ \mu\mathrm{s}$ to $20\ \mu\mathrm{s}$ in the helium cases (Table 4). Since the acquisition rate is $3.33\ \mathrm{Hz}$, the database is interpreted as statistically independent snapshots rather than time-resolved trajectories. This choice is sufficient for ensemble and conditional statistics, but it does not allow event sequencing in time.

$\mathbf{N_2}$			
Re	2000	4000	6000
Δt_{PIV} (μs)	140	70	40
He			
Re	720	1440	2160
Δt_{PIV} (μs)	55	30	20

Table 4. PIV inter-frame timing for N_2 and He jets at matched momentum flux. Δt_{PIV} denotes the time between laser pulses in double-frame acquisition.

2.2. PLIF measurements and laser-sheet correction

Planar Laser-Induced Fluorescence (PLIF) is used to measure the scalar concentration field. Anisole is selected as fluorescent tracer because it provides a high quantum yield at low seeding fractions, minimizing its influence on the mixture properties. The tracer is excited at $\lambda = 266\ \mathrm{nm}$ using a Nd:YAG laser (Quantel 850) delivering approximately $100\ \mathrm{mJ}$ per pulse. A dichroic mirror combines the PLIF and PIV beams before the laser sheet is formed. To suppress Mie scattering at $266\ \mathrm{nm}$ from the DEHS particles while preserving anisole fluorescence, a liquid filter composed of 95% iso-octane and 5% toluene is used (Pasquier et al., 2007). The fluorescence signal is collected by a PIMAX 4 intensified CCD camera coupled to a Cerco $100\ \mathrm{mm}$, $f/2.8$ UV lens. The PLIF acquisition is synchronized with the PIV system, so that scalar and velocity fields are available for the

same instantaneous realizations. The measured PLIF signal depends on the optical setup, including intensified CCD cameras, which are influenced by factors such as light intensity and camera gain. To ensure accurate calibration, it is essential to verify the linearity of fluorescence and CCD response by varying anisole concentration and the laser energy. Linearity is critical for shot-to-shot correction, as calculations involve simple cross-multiplications. For calibration, we conducted tests using 100 images of a laminar jet while adjusting the parameters mentioned. First, the sensitivity of the anisole concentration was evaluated, revealing a linear range between 0.001% and 0.03% (Figure 3a), beyond which the Beer-Lambert effect becomes significant, so it was decided to stay in the middle at 0.02%. Then, the results showed a linear response of fluorescence to laser energy, with measurements limited to 100 mJ/shot (Figure 3b). We therefore kept the laser at maximum power to maximize shot-to-shot stability.

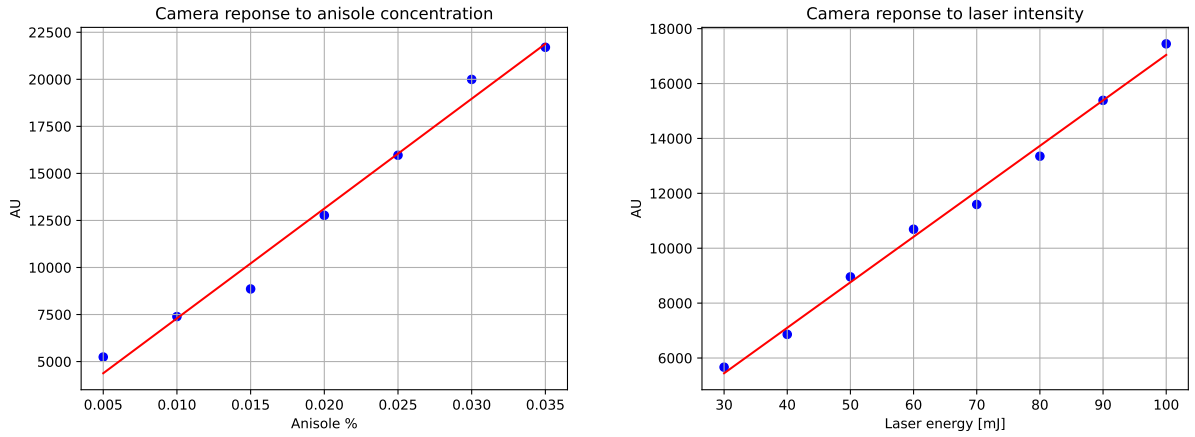
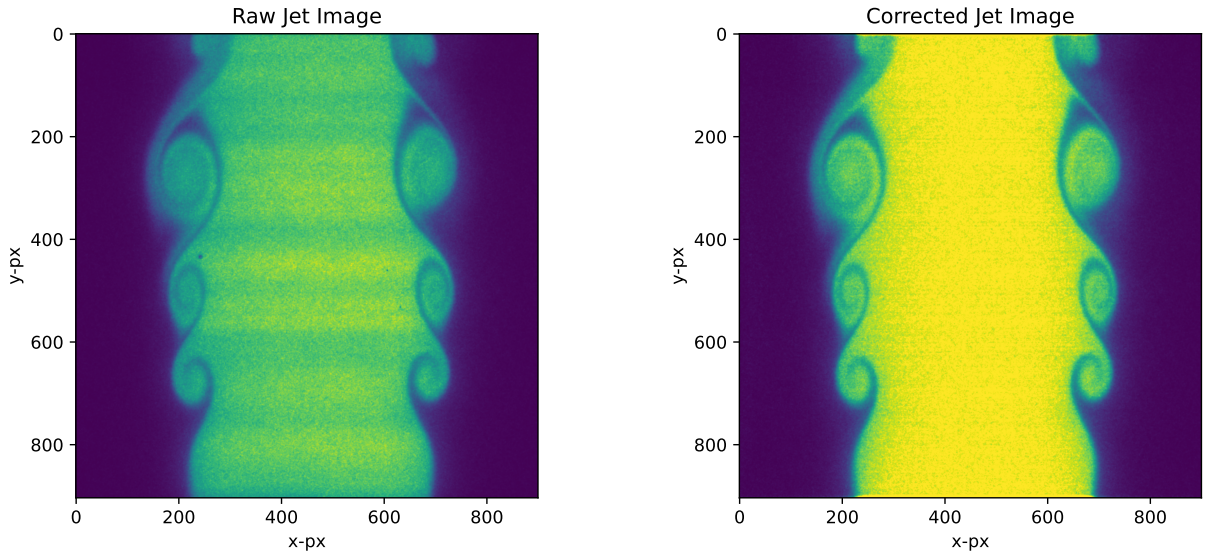


Figure 3. Camera response to anisole concentration (a) and laser intensity (b).

Because PLIF is sensitive to spatial laser-sheet inhomogeneity and shot-to-shot energy fluctuations, a correction procedure is applied before concentration statistics are computed. The method is based on a synthetic-sheet reconstruction adapted from Voivenel (2016). A reference laser-sheet profile is measured through an ethanol cuvette, and a pixel-wise correspondence is established between the cuvette camera and the jet camera. The cuvette image is then transformed into the jet-camera frame and used to correct spatial inhomogeneities. A secondary normalization based on a reference region inside the jet potential core accounts for shot-to-shot laser energy variations. The procedure removes horizontal illumination bands and restores a more uniform concentration level inside the jet core as seen in Figure 4.



(a) Raw jet image **(b)** Corrected jet image

Figure 4. PLIF images before and after the correction process.

3. Methodology

3.1. Detection of coherent structures

The structure conditioned analysis begins by detecting coherent scalar structures associated with Kelvin–Helmholtz (KH) instabilities. These features originate near the turbulent/non-turbulent interface (TNTI) in the early shear layer. A reference KH structure is manually selected from a PLIF image by defining a rectangular region of interest (ROI) that contains a representative scalar feature. This ROI is used as the *template*.

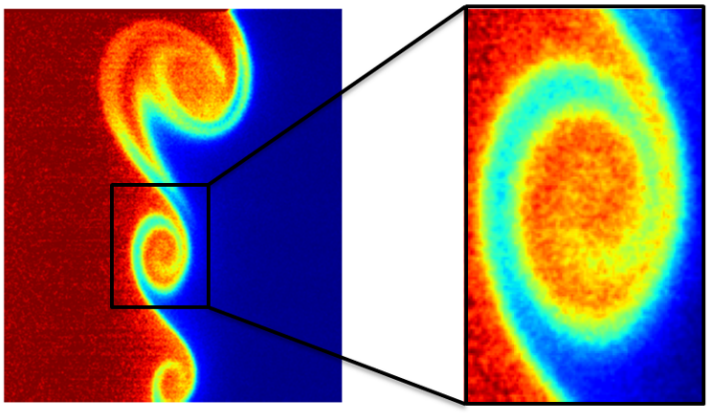


Figure 5. Example of a coherent structure used as a template (Kelvin–Helmholtz instability) and the image from which it was extracted.

For each PLIF frame, similar structures are identified by computing the correlation coefficient between the template and candidate patches. In order to focus on physically meaningful structures, the matching is performed inside a horizontal band centered around the TNTI, and only the best match in the subregion is retained. A patch is accepted if the correlation coefficient exceeds $R > 0.92$. This threshold represents a compromise between rejecting spurious detections and retaining a sufficient number of events for converged statistics. Sensitivity tests with nearby thresholds showed that the ordering of the dominant budget terms remains unchanged; the primary effect of the threshold is the number of retained structures and thus the statistical convergence of the conditioned averages.

Each valid match is extracted and stored. The PLIF patch provides the scalar organization of the structure, while the synchronized PIV frame provides the co-located velocity field needed for the TKE budget. The number of retained structures depends on both Reynolds number and gas configuration. Table 5 reports the detections retained with $R > 0.92$. The general reduction of matches with increasing Reynolds number reflects stronger mixing and a less repeatable interface topology at higher turbulence intensity. The N_2/N_2 case at $Re = 4000$ is an exception, because the selected template produced fewer high correlation matches than the templates used for the other nitrogen cases.

Jet	$Re = 2000$	$Re = 4000$	$Re = 6000$
N_2/N_2	4625	169	1016
He/N_2	1410	621	66

Table 5. Number of matched coherent structures for each flow condition ($R > 0.92$).

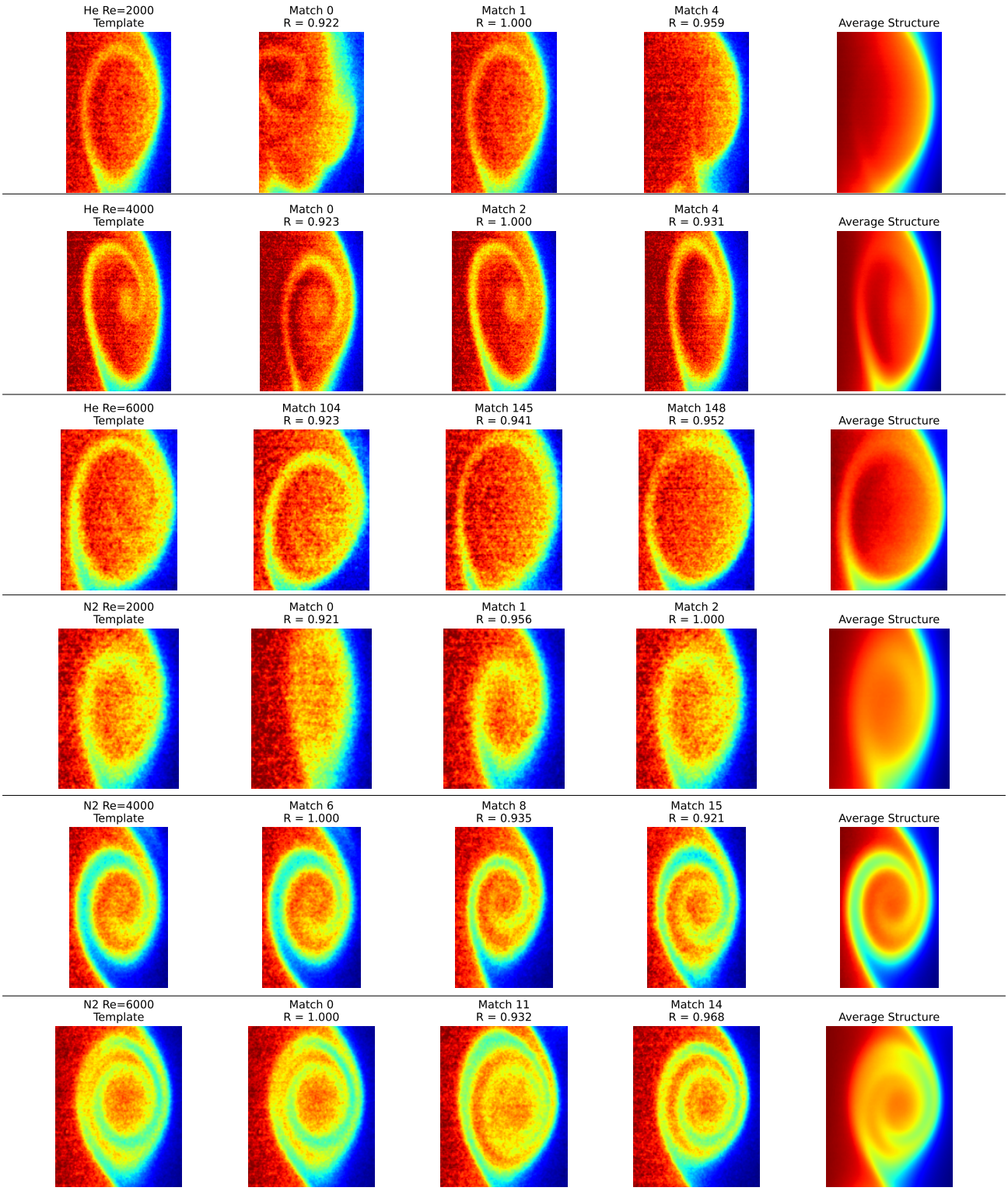


Figure 6. Visualization of the matching results used to extract coherent structures in round jets. Each row corresponds to a different case (gas and Reynolds number). The first column shows the structure template used for detection; the next three columns show individual matched regions with the highest correlation scores; the final column displays the mean of all matched patches.

3.2. Field extraction and structure conditioned statistics

Once a coherent structure is detected in the scalar field, the corresponding matched pixel coordinates are used to extract a co-located velocity patch from the synchronized PIV data. The PIV and PLIF measurements are spatially and temporally synchronized; therefore, no additional registration is required after the common calibration procedure. For each match, a fixed size window is extracted and stored in a local coordinate system attached to the template. Ensemble averages of these windows provide structure conditioned scalar, velocity and TKE budget fields. This local reference frame suppresses the smearing caused by event wandering in the laboratory frame and emphasizes recurrent spatial patterns associated with the coherent structure.

The global statistics and the structure-conditioned statistics answer complementary questions. Global averages describe the mean organization of the jet in the laboratory frame, including the mean shear layer and its Reynolds number evolution. Structure-conditioned averages describe what the local energy balance looks like when the observer follows a repeated event. In the figures below, global maps retain the physical axes (r, y), where y is measured from the jet exit and r from the centerline. Structure-conditioned maps are shown in patch coordinates; their axes therefore indicate the local window size and not the absolute position in the jet.

3.3. Turbulent kinetic energy budget equation

The axisymmetric TKE budget is written in cylindrical coordinates for statistically stationary, low Mach number round jets with no mean swirl. The formulation follows the axisymmetric framework used by Krawczynski (2007). For the constant density N_2/N_2 jet, classical Reynolds averaging is used. The steady equation reads

$$\overbrace{V\frac{\partial k}{\partial y}+U\frac{\partial k}{\partial r}}^{\text{Advection}}=\overbrace{-\left[\overline{uv}\left(\frac{\partial V}{\partial r}+\frac{\partial U}{\partial y}\right)+\left(\overline{v^2}-\overline{u^2}\right)\frac{\partial V}{\partial y}\right]}^{\text{Production}} \overbrace{-\frac{1}{r}\frac{\partial}{\partial r}\left(r\overline{T_r}\right)-\frac{\partial \overline{T_y}}{\partial y}}^{\text{Turbulent diffusion}}-\overbrace{\varepsilon}^{\text{Dissipation}}+\overbrace{R}^{\text{Residual}}, \tag{1}$$

with

$$k=\frac{1}{2}\left(2\overline{u^2}+\overline{v^2}\right)=\frac{1}{2}q^2, \tag{2}$$

$$\overline{T_r}=\frac{1}{2}\overline{q^2u}, \qquad \overline{T_y}=\frac{1}{2}\overline{q^2v}. \tag{3}$$

Here U and V are the mean radial and axial velocities, respectively, and u and v are the associated fluctuations. The production term includes the classical shear production contribution and the anisotropy contribution linked with axial strain. Turbulent diffusion is written in divergence form

with radial and axial components, so that positive and negative regions represent local export or import of TKE.

For the variable density He/N_2 jet, density fluctuations are important inside the shear layer. The TKE equation is therefore formulated with Favre averaging (Favre, 1958), $\widetilde{\phi} = \overline{\rho\phi}/\overline{\rho}$ and $\phi'' = \phi - \widetilde{\phi}$. The steady Favre-formulated equation used here is

$$\overbrace{\overline{\rho}\left(V\frac{\partial k}{\partial y} + U\frac{\partial k}{\partial r}\right)}^{\text{Advection}} = \overbrace{-\overline{\rho}\left[\widetilde{uv}\left(\frac{\partial V}{\partial r} + \frac{\partial U}{\partial y}\right) + \left(\widetilde{v^2} - \widetilde{u^2}\right)\frac{\partial V}{\partial y}\right]}^{\text{Production}} \overbrace{-\frac{1}{r}\frac{\partial}{\partial r}\left(r\widetilde{T}_r\right) - \frac{\partial \widetilde{T}_y}{\partial y}}^{\text{Turbulent diffusion}} - \overbrace{\overline{\rho}\,\widetilde{\varepsilon}}^{\text{Dissipation}} + \overbrace{R}^{\text{Residual}}, \tag{4}$$

with

$$k = \frac{1}{2}\left(2\widetilde{u^2} + \widetilde{v^2}\right) = \frac{1}{2}\widetilde{q^2}, \tag{5}$$

$$\widetilde{T}_r = \frac{1}{2}\widetilde{q^2 u}, \qquad \widetilde{T}_y = \frac{1}{2}\widetilde{q^2 v}. \tag{6}$$

Favre moments are computed from synchronized velocity density fields. Spatial derivatives are evaluated with centered second-order finite differences.

The dissipation is estimated using the locally axisymmetric surrogate of George & Hussein (1991),

$$\langle\varepsilon\rangle_{\text{axi}} = \nu\left[-\left\langle\left(\frac{\partial v}{\partial y}\right)^2\right\rangle + 2\left\langle\left(\frac{\partial v}{\partial r}\right)^2\right\rangle + 2\left\langle\left(\frac{\partial u}{\partial y}\right)^2\right\rangle + 8\left\langle\left(\frac{\partial u}{\partial r}\right)^2\right\rangle\right], \tag{7}$$

where $\nu = \mu/\rho$ is constant for the N_2/N_2 case and local for the He/N_2 case. A small radius floor is imposed near the jet axis to avoid numerical singularities. Pressure diffusion is not measured directly. The residual R is computed as the pointwise imbalance of the explicitly evaluated terms and therefore contains pressure transport, unresolved azimuthal contributions, finite-difference errors, surrogate dissipation limitations and measurement noise.

4. Results

4.1. Two-dimensional TKE-budget fields

Figure 7 presents the N_2/N_2 TKE-budget maps at $Re = 2000$, 4000 and 6000. For each Reynolds number, the top row shows the global average and the bottom row shows the average conditioned on coherent structures. In the global fields, dissipation forms a narrow band that follows the mean shear layer and intensifies downstream with increasing Reynolds number. In the fields

conditioned on detected structures, the dissipation footprint collapses into more localized sheets attached to the detected interfaces, demonstrating that a large part of the apparent global thickness is produced by event wandering. Production is globally organized as a mixed-sign ridge along the shear layer, with positive and negative lobes set by local shear and strain. Conditioning concentrates this production into compact hot spots around the coherent structure. Advection and turbulent diffusion have broader footprints in the global frame, while in the structure frame they appear as adjacent positive and negative lobes, indicating intense local redistribution of k around the coherent event.

The Reynolds number trend is clear in all nitrogen terms. Dissipation and production become stronger and more elongated along the shear layer, while the conditioned maps show that the local structure remains organized around interface-tied sheets and lobes. The most pronounced Reynolds number amplification occurs in the transport terms: global advection grows with the downstream footprint, whereas conditioned advection reaches large alternating extrema inside the patch. Turbulent diffusion also develops stronger positive/negative bands.

Figure 8 shows the corresponding He/N_2 fields. The variable density jet exhibits a broader and more asymmetric budget organization than the constant density case. In the global fields, dissipation spreads around the mean shear layer and local extrema are larger because the helium jet has higher velocities at matched momentum flux. The maps obtained by conditioning on detected structures again sharpen dissipation into sheets, but the patch organization is less symmetric than in N_2/N_2. Production is concentrated near the detected interface and can display stronger negative lobes. Advection and turbulent diffusion show the largest local variability: the global fields contain broad footprints, while the conditioned fields reveal intense neighboring lobes that reflect event-wise transport across the interface and along the coherent structure.

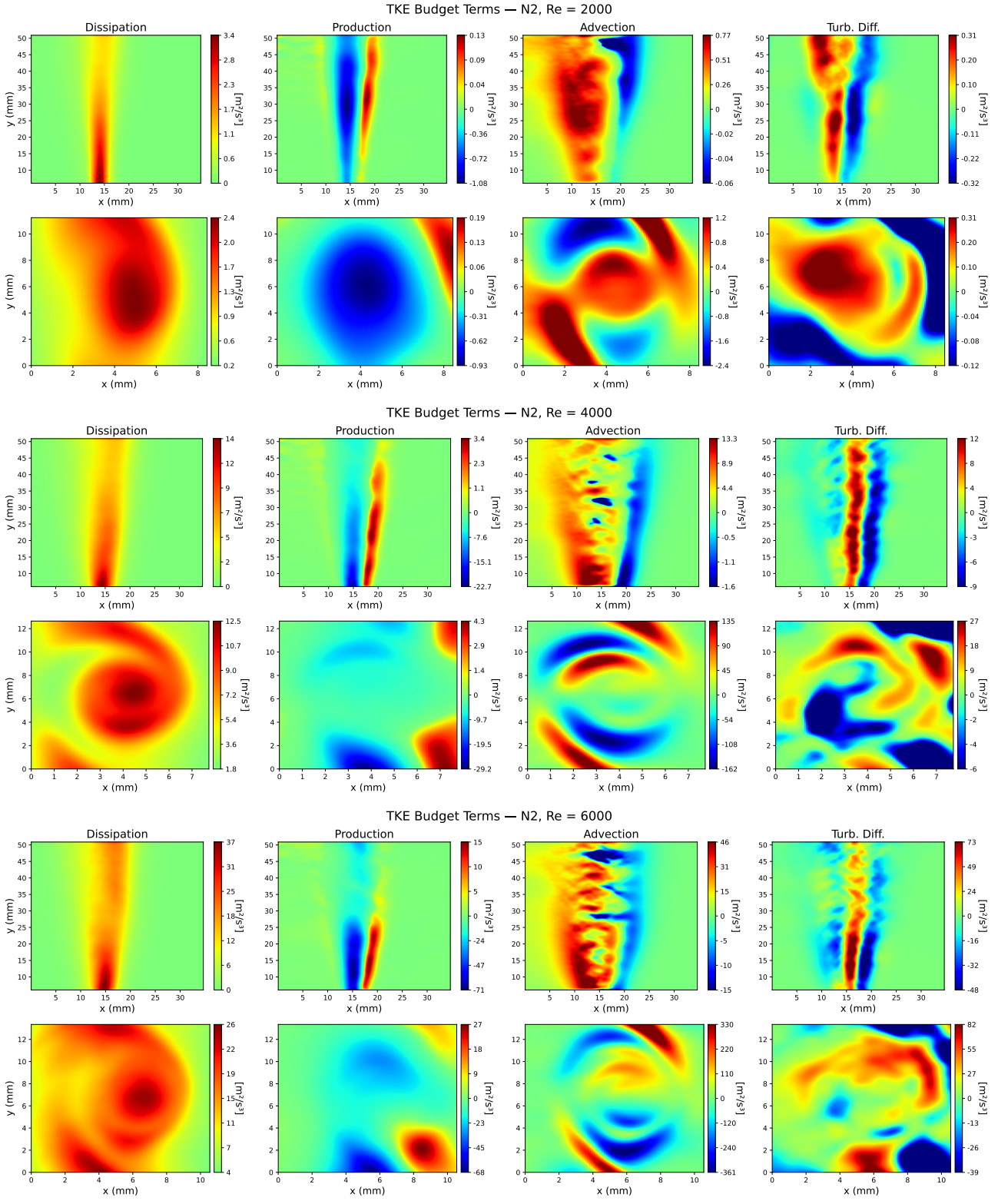


Figure 7. TKE-budget terms in the N_2 jet at $Re = 2000$ (top), $Re = 4000$ (middle), and $Re = 6000$ (bottom). Top row: global averages. Bottom row: fields conditioned on detected structures.

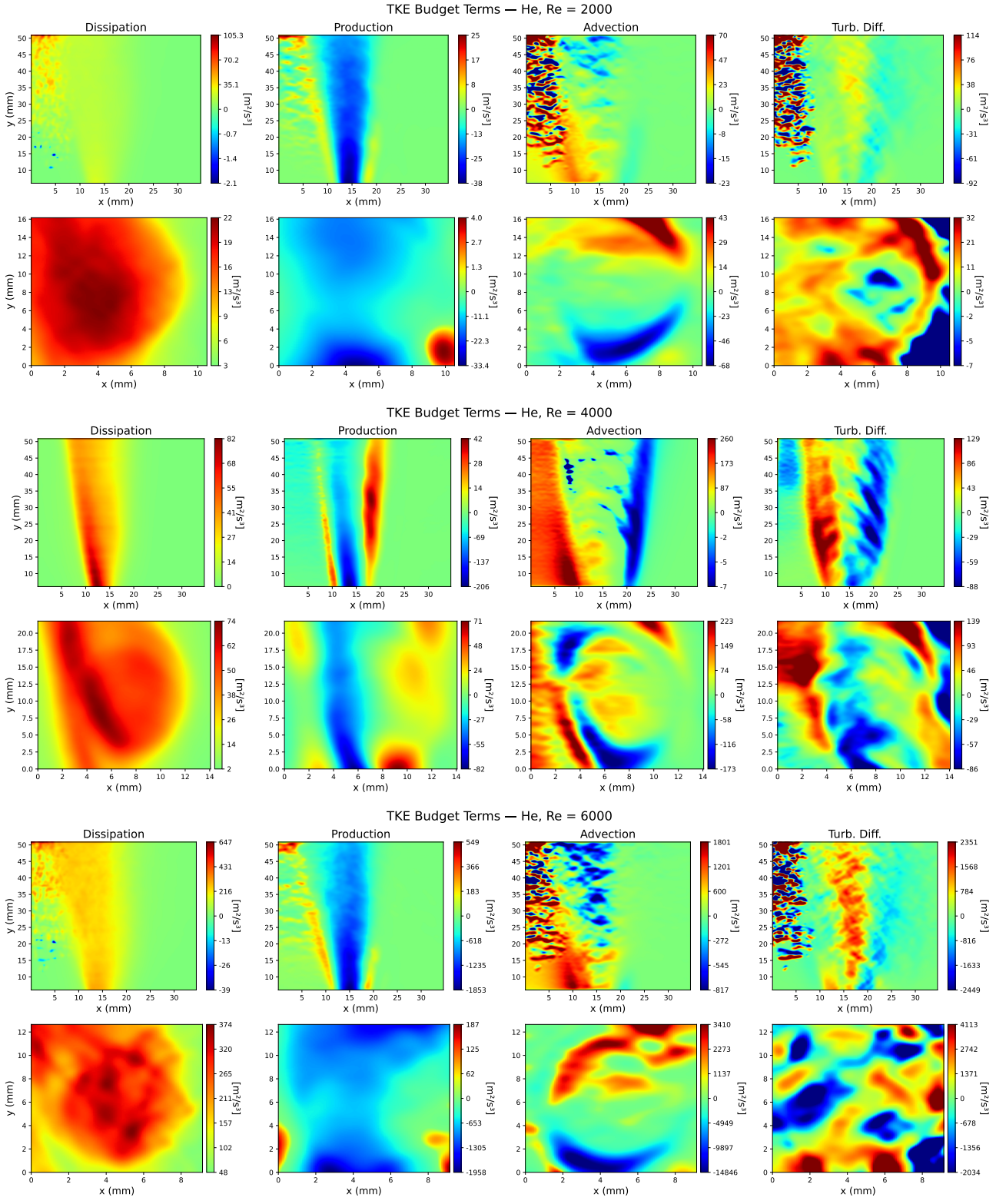


Figure 8. TKE-budget terms in the He jet at $Re = 2000$ (top), $Re = 4000$ (middle), and $Re = 6000$ (bottom). Top row: global averages. Bottom row: fields conditioned on detected structures.

Overall, structure conditioning systematically sharpens dissipation and production in both gases. The method also reveals that transport terms, which are partially smeared by global averaging, can dominate the local event-scale balance. Variable density amplifies the asymmetry and magnitude of the local budget, particularly in advection and turbulent diffusion. This behaviour suggests that helium/nitrogen shear-layer structures are not only geometrically larger, but also dynamically more active in redistributing TKE around the TNTI.

4.2. Localized budget contributions

To quantify the local balance of the TKE budget, the five contributions are sampled at representative positions and displayed as normalized stacked bars. Each bar contains production P, advection A, turbulent diffusion T, dissipation $-\varepsilon$, and a pressure-diffusion/residual contribution P_p. For the global fields, three radial positions are sampled across the jet: Jet side, Shear/Center and Coflow side. For the fields conditioned on detected structures, the same labels denote three positions inside the local patch. Each term is averaged over the chosen column or over a 5×5 subwindow, and the algebraic vector $[P, A, T, P_p, -\varepsilon]$ is normalized by the sum of absolute magnitudes. This normalization emphasizes relative local activity rather than dimensional magnitude. Positive slices indicate local sources or export of TKE, while negative slices indicate sinks or import.

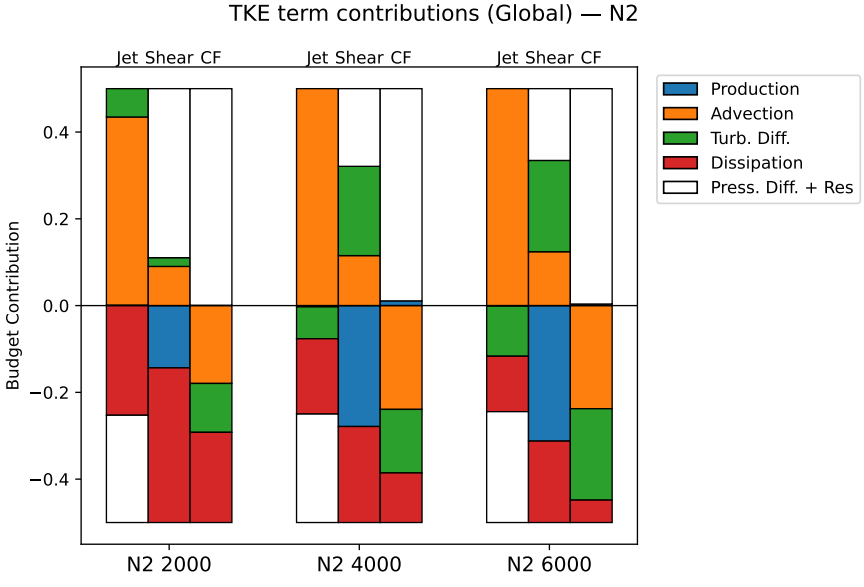


Figure 9. Normalized TKE-budget term fractions at three positions inside the windows centered on coherent structures (Jet side, Center, Coflow side) for the N_2/N_2 jet at $Re = 2000$, 4000, and 6000. Each bar is normalized by the sum of absolute local means; heights indicate fractions of local activity, and negative slices appear below zero.

For the global N_2/N_2 fields (Fig. 9), advection dominates the positive side near the jet side for all

Reynolds numbers. Away from the jet core, advection weakens and the positive balance increasingly relies on the pressure-diffusion/residual contribution. Dissipation is consistently a major negative term, especially at the shear/center position and toward the coflow side. Turbulent diffusion remains weaker in the global sampling, with small positive or negative contributions depending on position. Production is comparatively small in these local columns and frequently appears on the negative side at the shear/center position, reflecting the local sign of the strain-production combination.

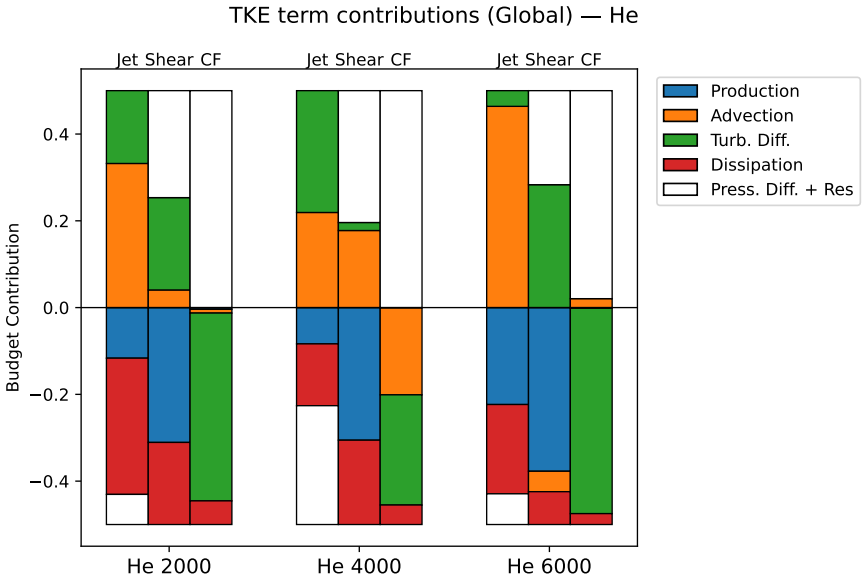


Figure 10. normalized TKE-budget term fractions at three positions inside the windows centered on coherent structures (Jet side, Center, Coflow side) for the He/N_2 jet at $Re = 2000, 4000$, and 6000. Each bar is normalized by the sum of absolute local means; heights indicate fractions of local activity, and negative slices appear below zero.

In the global He/N_2 bars (Fig. 10), the positive share is carried mainly by advection on the jet side, whereas the shear/center and coflow positions rely more strongly on pressure diffusion plus residual. Turbulent diffusion grows with radius and can become a major negative contribution at the coflow edge. At the highest Re case, advection and turbulent diffusion become particularly large, confirming that variable density transport dominates the local balance when the jet velocity and scalar gradients are strongest. Production remains modest overall and is usually negative at the shear/center position.

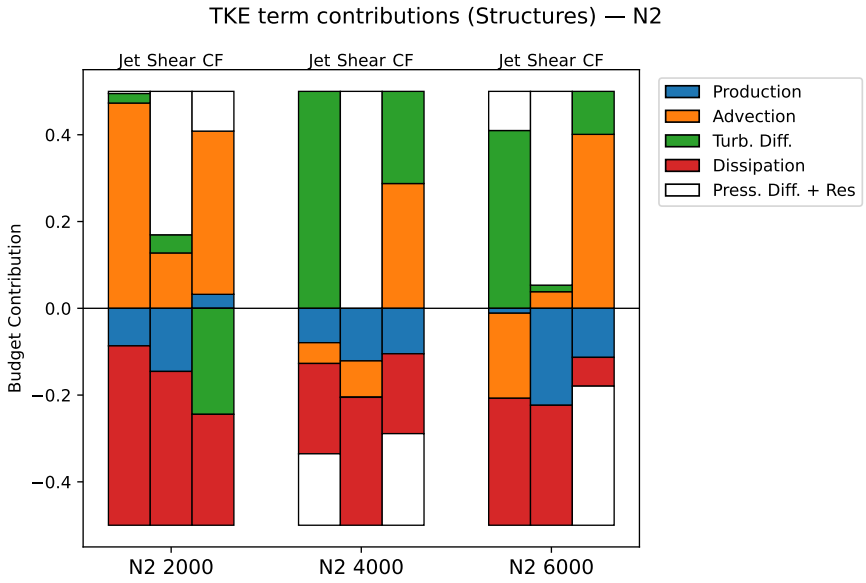


Figure 11. Normalized, TKE-budget term fractions at three positions inside the windows centered on coherent structures (Jet side, Center, Coflow side) for the N_2/N_2 jet at $Re = 2000$, 4000, and 6000. Each bar is normalized by the sum of absolute local means; heights indicate fractions of local activity, and negative slices appear below zero.

For the N_2/N_2 fields conditioned on coherent structures (Fig. 11), the partition differs from the global one because the sampling follows the coherent structure. At $Re = 2000$, advection dominates the positive side on the jet and coflow sides, while dissipation dominates the negative side. At the center of the patch, a positive pressure-diffusion/residual contribution appears together with advection, suggesting that the unresolved pressure transport and closure terms are concentrated close to the structure core. As Re increases, turbulent diffusion becomes more prominent on the jet side, while advection remains important toward the coflow side. Dissipation remains the most robust negative contribution across positions, confirming that the detected structure organizes a local sink of TKE around its interface.

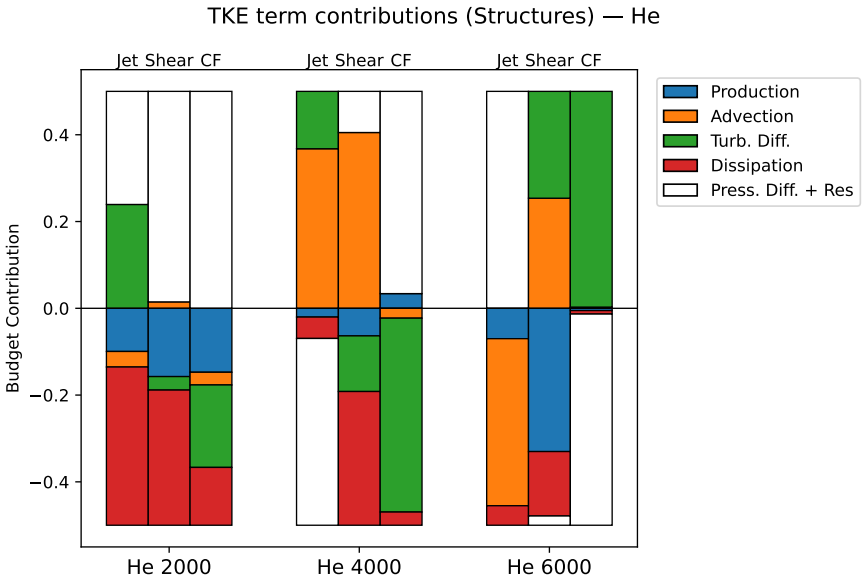


Figure 12. normalized, sign-preserving TKE-budget term fractions at three positions inside the windows centered on coherent structures (Jet side, Center, Coflow side) for the He/N_2 jet at $Re = 2000, 4000$, and 6000. Each bar is column-normalized by the sum of absolute local means; heights indicate fractions of local activity, and negative slices appear below zero.

For the He/N_2 fields conditioned on coherent structures (Fig. 12), the local balance is more asymmetric and more sensitive to Reynolds number. At the lowest matched-momentum case, dissipation dominates the negative side across the window, while pressure diffusion plus residual supplies much of the positive side, especially near the jet and coflow positions. At intermediate Reynolds number, advection becomes dominant on the positive side at the jet and center positions, while turbulent diffusion and dissipation define most of the negative balance. At the highest case, pressure diffusion plus residual becomes very large on the jet and coflow sides, whereas the center position is shared by advection and turbulent diffusion on the positive side and production/dissipation on the negative side. These bars emphasize that variable density increases the importance of transport and closure terms in the local structure frame.

The stacked bar analysis clarifies the difference between global views and views obtained by conditioning on coherent structures. In global fields, advection is strongest near the jet side and weakens toward the coflow edge, while pressure-diffusion/residual terms often compensate the remaining imbalance away from the core. In fields conditioned on coherent structures, turbulent diffusion and advection reorganize around the coherent event and may become locally dominant. Dissipation consistently occupies most of the negative side, confirming that coherent structures are not only scalar or vortical patterns, but also local organizers of TKE sinks and transport pathways.

5. Conclusions

This paper is a structure-conditioned analysis of axisymmetric TKE budgets in the near field of constant- and variable density round jets. The experimental database combines synchronized PIV and PLIF measurements in N_2/N_2 and He/N_2 jets at matched momentum flux. Coherent structures associated with Kelvin–Helmholtz structures are detected by template matching in the PLIF fields, and co-located PIV windows are extracted to compute local TKE-budget terms in this reference frame. TKE-budget activity concentrates near the shear layer and intensifies with Reynolds number in both configurations. Structure conditioning consistently sharpens dissipation and production into sheets close to the interface and compact hot spots, demonstrating that global averages hide part of the local event-scale organization. Advection and turbulent diffusion become neighboring positive/negative lobes in the conditioned frame, showing that coherent structures redistribute TKE across and along the TNTI. Variable density amplifies asymmetry and strengthens transport terms, particularly in the helium jet, where advection and turbulent diffusion often dominate the local balance. Finally, the pressure-diffusion/residual contribution remains significant, especially near conditioned structure cores and in the variable density case, indicating the importance of pressure transport, unresolved three-dimensional effects and closure limitations. These observations have implications for reduced models and closures of shear-layer turbulence. Models that distribute production or dissipation only according to global mean gradients may miss the fact that much of the exchange is organized around intermittent coherent structures. A budget conditioned on coherent structures therefore provides a useful target for LES/RANS closures and for future comparisons with time-resolved or volumetric measurements. Future work should include alternative templates, orientation/phase alignment, and three dimensional measurements or DNS/LES databases to isolate pressure diffusion, recover missing gradients and follow the temporal sequence of coherent events.

References

Favre, A. (1958). Équations statistiques des gaz turbulents: masse, quantité de mouvement. *Comptes Rendus Hebdomadaires des Séances de l'Académie des Sciences*, *246*, 2576–2579.

George, W. K., & Hussein, A. K. (1991). Locally axisymmetric turbulence. *Journal of Fluid Mechanics*, *233*, 1–23. doi: 10.1017/S0022112091000196

Krawczynski, J.-F. (2007). *La structure du champ de vitesse dans un réacteur à jets opposés. caractérisation du mélange turbulent* (Doctoral dissertation). Retrieved from `http://www.theses.fr/2007ROUES071` (Thèse de doctorat dirigée par Danaila, Luminita Sciences pour l'ingénieur. Énergétique Rouen 2007)

Neamtu-Halic, M. M., Krug, D., Mollicone, J.-P., van Reeuwijk, M., Haller, G., & Holzner, M. (2020). Connecting the time evolution of the turbulence interface to coherent structures. *Journal of Fluid Mechanics*, *898*, A3. Retrieved from https://doi.org/10.1017/jfm.2020.414 doi: 10.1017/jfm.2020.414

Pasquier, N., lecordier, B., & Cessou, A. (2007). Investigation of flame propagation through a stratified mixture by simultaneous piv/lif measurements. In *Proceedings of the combustion institue.*

van Reeuwijk, M., Vassilicos, J. C., & Craske, J. (2021). Unified description of turbulent entrainment. *Journal of Fluid Mechanics*, *908*, A12. Retrieved from https://doi.org/10.1017/jfm.2020.836 doi: 10.1017/jfm.2020.836

Voivenel, L. (2016). *Influence of the hydrodynamic parameters on turbulment mixing of heterogeneous fluids. analytical and experimental study* (Unpublished doctoral dissertation). Normandie Université, Insa de Rouen.

Zhou, Y., & Vassilicos, J. C. (2020). The energy cascade at the turbulent/non-turbulent interface. *Physical Review Fluids*, *5*(6), 064604. Retrieved from https://doi.org/10.1103/PhysRevFluids.5.064604 doi: 10.1103/PhysRevFluids.5.064604